

# Characterizing Multi-Subevent Earthquakes Using the Brune Source Model

Meichen Liu<sup>1,1</sup>, Yihe Huang<sup>1,1</sup>, and Jeroen Ritsema<sup>1,1</sup>

<sup>1</sup>University of Michigan

November 30, 2022

## Abstract

Although the Brune source model describes earthquake moment release as a single pulse, it is widely used in studies of complex earthquakes with multiple episodes of high moment release (i.e., multiple subevents). In this study, we investigate how corner frequency estimates of earthquakes with multiple subevents are biased if they are based on the Brune source model. By assuming complex sources as a sum of multiple Brune sources, we analyze 1,640 source time functions (STFs) of Mw 5.5-8.0 earthquakes in the SCARDEC catalog to estimate the corner frequencies, onset times, and seismic moments of subevents. We identify more subevents for strike-slip earthquakes than dip-slip earthquakes, and the number of resolvable subevents increases with magnitude. We find that earthquake corner frequency correlates best with the corner frequency of the subevent with the highest moment release (i.e., the largest subevent). This suggests that, when the Brune model is used, the estimated corner frequency and therefore the stress drop of a complex earthquake is determined primarily by the largest subevent rather than the total rupture area. Our results imply that the stress variation of asperities, rather than the average stress change of the whole fault, contributes to the large variance of stress drop estimates.

## Hosted file

supporting\_information.docx available at <https://authorea.com/users/529038/articles/608987-characterizing-multi-subevent-earthquakes-using-the-brune-source-model>

1           **Characterizing Multi-Subevent Earthquakes Using the Brune Source Model**

2   **Meichen Liu<sup>1</sup>, Yihe Huang<sup>1</sup>, and Jeroen Ritsema<sup>1</sup>**

3   <sup>1</sup>Department of Earth and Environmental Sciences, University of Michigan, Ann Arbor, MI,  
4   USA.

5   Corresponding author: M. Liu (meichenl@umich.edu)

6   **Key Points:**

- 7           • We use global source time functions to investigate the Brune source parameters of multi-  
8           subevent earthquakes
- 9           • We find that the master event corner frequencies correlate better with those of the large  
10          subevent
- 11          • The Brune stress drop is better correlated with the stress change of the asperity with the  
12          largest moment release
- 13

14 **Abstract**

15 Although the Brune source model describes earthquake moment release as a single pulse, it is  
16 widely used in studies of complex earthquakes with multiple episodes of high moment release  
17 (i.e., multiple subevents). In this study, we investigate how corner frequency estimates of  
18 earthquakes with multiple subevents are biased if they are based on the Brune source model. By  
19 assuming complex sources as a sum of multiple Brune sources, we analyze 1,640 source time  
20 functions (STFs) of Mw 5.5-8.0 earthquakes in the SCARDEC catalog to estimate the corner  
21 frequencies, onset times, and seismic moments of subevents. We identify more subevents for  
22 strike-slip earthquakes than dip-slip earthquakes, and the number of resolvable subevents  
23 increases with magnitude. We find that earthquake corner frequency correlates best with the  
24 corner frequency of the subevent with the highest moment release (i.e., the largest subevent).  
25 This suggests that, when the Brune model is used, the estimated corner frequency and therefore  
26 the stress drop of a complex earthquake is determined primarily by the largest subevent rather  
27 than the total rupture area. Our results imply that the stress variation of asperities, rather than the  
28 average stress change of the whole fault, contributes to the large variance of stress drop  
29 estimates.

30 **Plain Language Summary**

31 The Brune source model, which describes earthquakes as a single pulse of energy release with  
32 time, is widely used to study earthquake sources regardless of the true source process. However,  
33 multiple energy-release pulses, termed subevents for an earthquake, are not uncommon. The  
34 Brune source is characterized by its corner frequency that is related to the inverse of source  
35 duration. The frequency spectrum begins to decay at the corner frequency, thereby controlling  
36 the hazardous high-frequency ground motions. In this study, we explore the relationship between  
37 the corner frequency of an earthquake and corner frequencies of its subevents. Assuming each  
38 subevent is a Brune source, we extract corner frequencies of subevents for 1,640 earthquakes  
39 recorded in a global dataset, and find the earthquake corner frequency is closely related to the  
40 corner frequency of the subevent with the highest energy release. It indicates that the stress  
41 release converted from the Brune-source corner frequency of an earthquake represents the stress  
42 release in the source region of its largest subevent rather than of the entire earthquake. Our  
43 findings improve interpretation of the corner frequency obtained from the Brune source model  
44 and help explain the large uncertainty of stress release estimates.

45  
46

## 47 **1 Introduction**

48           The classical earthquake source model proposed by J. Brune more than five decades ago  
49 (Brune, 1970) is still widely used to understand the initiation of faulting, the propagation of a  
50 fault rupture, and the radiation of seismic energy. In the Brune model, a circular crack  
51 instantaneously experiences a shear dislocation due to a constant stress drop (i.e., the change of  
52 stress) on the fault. The Brune model links three key elements of an earthquake: the seismic  
53 moment, corner frequency, and stress drop with simple functions in which the seismic moment  
54 and corner frequency are the two free parameters. The Brune model predicts that the source  
55 spectrum is constant at frequencies lower than the corner frequency, and decays proportional to  
56 the square of frequency at frequencies higher than the corner frequency, an important feature for  
57 the calculation of high-frequency ground motions for engineering applications (Papageorgiou  
58 and Aki, 1983; Purvance and Anderson, 2003; Sotiriadis et al., 2021). Numerous studies of small  
59 and large, shallow and deep, tectonic and induced earthquakes using regional and teleseismic  
60 data are based on the Brune source model when estimating stress drops (e.g., Abercrombie,  
61 1995; Garcia et al., 2004; Allmann & Shearer, 2009; Baltay et al., 2011; Oth, 2013; Chen &  
62 Shearer, 2018; Huang et al., 2016; Ruhl et al., 2017; Prieto et al., 2017; Trugman et al., 2017;  
63 Wu et al., 2018; Shearer et al., 2019; Liu et al., 2020; Yu et al., 2021).

64           Nevertheless, it is well recognized that earthquakes are complex on a wide variety of  
65 spatial and temporal scales. The barrier (Das and Aki, 1977) and asperity (Lay and Kanamori,  
66 1981; Lay et al., 1982) models describe stress and frictional differences on the fault plane. The  
67 rupture velocity and the moment rate during rupture expansion can change due to dynamic waves  
68 in fault damage zones (e.g., Huang and Ampuero, 2011) as well as fault curvature and  
69 segmentation (e.g., Ando and Kaneko, 2018; Ulrich et al., 2019). The complexity of rupture  
70 processes is evident for  $M_w > 7$  earthquakes (e.g., Ye et al. 2016; Hayes, 2017) but also for  
71 smaller earthquakes (e.g., Boatwright, 1984). Using local seismic arrays, moment rate  
72 fluctuations have been observed for  $M_w < 3.5$  earthquakes in the Charlevoix, Quebec seismic  
73 zone (Li et al., 1995; Fischer, 2005), on the San Andreas Fault (Wang et al., 2014; Abercrombie,  
74 2014; Abercrombie et al., 2020), and in the 2008 Mogul, Nevada swarm (Ruhl et al., 2017).  
75 Danré et al. (2019) used the Gaussian source model to systematically analyze the source  
76 complexity for SCARDEC STFs. They observed increasing source complexity with earthquake  
77 and an important scaling of the moment of subevent with the earthquake moment by a factor of  
78 0.8. For the Brune source model, the source complexity may cause earthquake source spectra to  
79 deviate from the frequency-squared spectral decay for moderate to large (e.g., Luco, 1985;  
80 Atkinson, 1993; Beresnew and Atkinson, 2001; Denolle and Shearer, 2016; Yin et al., 2021) and  
81 small earthquakes (e.g., Uchide and Imanishi, 2016). The Brune source model has also been  
82 modified to include two corner frequencies to explain the deviation (Archuleta & Ji, 2016;  
83 Denolle and Shearer, 2016; Uchide and Imanishi, 2016; Ji & Archuleta, 2021).

84           For many earthquakes, however, there are insufficient data to model source complexity.  
85 It is also not a common practice to use complex source models to predict earthquake ground

86 motions. Therefore, the Brune source model is still widely used to estimate source parameters  
 87 and ground motions regardless of earthquake source complexity. This poses a fundamental  
 88 question: What is measured by the Brune source model when it is applied to complex  
 89 earthquakes?

90 Here we investigate what kind of source properties are represented by the Brune source  
 91 model for earthquakes with multiple episodes of high moment release (i.e., multiple subevents).  
 92 We first quantify earthquake source complexity by analyzing the number and source properties  
 93 of subevents in source time functions (STFs) of hundreds of Mw 5.5 – 8.0 earthquakes in the  
 94 SCARDEC (Seismic source CHAracteristic Retrieved from DEConvolving teleseismic body  
 95 waves) catalog (Vallée and Douet, 2016). We describe and decompose the STF as a sum of  
 96 Brune sources, and estimate corner frequencies and seismic moments of subevents. By  
 97 comparing measured source complexity to that observed by Danré et al. (2019), we will further  
 98 understand the scaling relationship between the source complexity and the subevent moment. We  
 99 also derive the theoretical source spectrum of a complex earthquake with two Brune subevents.  
 100 Using both SCARDEC analysis and theoretical derivation, we compare the earthquake’s overall  
 101 corner frequency to the corner frequencies of individual subevents, and show how earthquake  
 102 corner frequency and stress drop depend on the temporal spacing and relative moments of  
 103 subevents.

## 104 2 Methods

### 105 2.1 Source Time Function decomposition

106 In the time domain, the Brune source is defined as

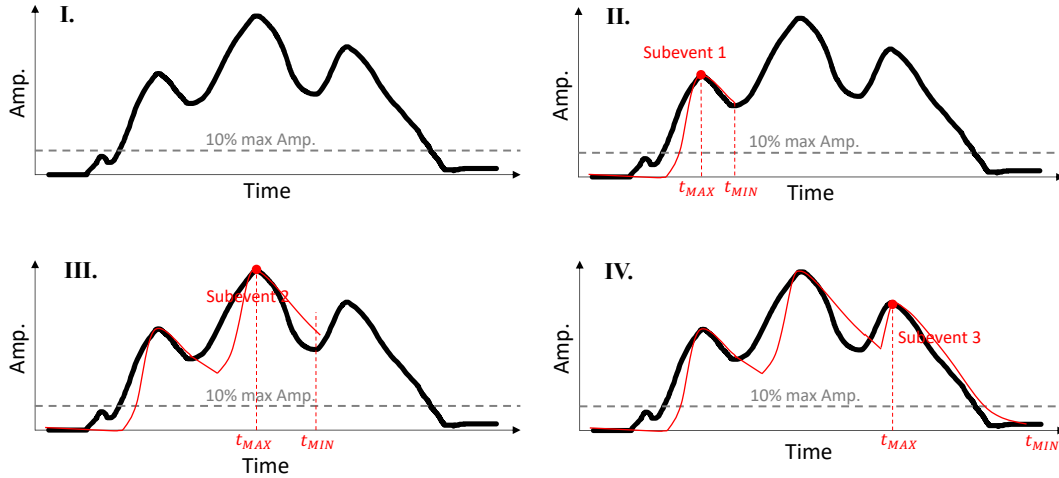
$$107 \quad \Omega(t, t_0, f_c, M_0) = M_0(2\pi f_c)^2(t - t_0)e^{-2\pi f_c(t-t_0)}H(t - t_0) \quad (1)$$

108 where  $H(t - t_0)$  is the Heaviside function,  $t_0$  is the onset time of the rupture,  $M_0$  is the seismic  
 109 moment, and  $f_c$  is the corner frequency that is scaled to a characteristic rupture time  $1 / f_c$ . The  
 110 Brune model predicts a far-field spectrum

$$111 \quad \Omega(f, f_c, M_0) = \frac{M_0}{1 + \frac{f^2}{f_c^2}} \quad (2)$$

112 which has a plateau at frequencies much lower than  $f_c$  and decreases proportional to  $f^2$  at  
 113 frequencies higher than  $f_c$ . The stress drop  $\Delta\sigma$  is proportional to  $f_c^3$  (Madariaga, 1976).

114 We call the Brune source that best matches the STF of an earthquake  $\Omega_{STF}$ . The seismic  
 115 moment and corner frequency of  $\Omega_{STF}$  are  $M_{STF}$  and  $f_{STF}$ , respectively. To determine  $M_{STF}$  and  
 116  $f_{STF}$  we transform the SCARDEC STF to the frequency domain using a Fast Fourier Transform  
 117 algorithm (Cooley and Tukey, 1965) and estimate  $f_{STF}$  in the frequency range of 0.01 – 2.0 Hz  
 118 using the trust-region-reflective least-square algorithm (Branch et al., 1999). For a complex STF  
 119 with multiple maxima,  $M_{STF}$  approximates the earthquake’s integrated moment rate, and  $f_{STF}$   
 120 represents an average value of the rupture duration.



121

122

123

124

Figure 1. Flowchart of STF decomposition that finds the best corner frequency of subevents that minimizes the misfit one by one in time series. See main text for detailed processes to locate subevents and fit corner frequencies.

125

126

To model a complex STF with multiple episodes of high moment rate (i.e., multiple subevents), we write the STF as a sum of Brune pulses:

127

$$\Omega_{SUM}(t) = \sum_{N=1}^{N_{ev}} \Omega_N(t, t_N, f_N, M_N) \quad (3)$$

128

129

130

131

132

133

134

135

136

137

138

139

140

141

142

143

To determine the number of resolvable Brune pulses in  $\Omega_{SUM}$ , we follow the iterative approach by Danré et al. (2019) with some modifications (Figure 1). There are three essential steps: i) To determine subevent  $N$ , find the time  $t_{MAX}$  of the  $N$  local maximum in the STF that is larger than 10% of the STF's maximum value to avoid overfitting small oscillations as individual subevents. Then we find the time  $t_{MIN}$  of the first local minimum in the STF more than 0.5 s after  $t_{MAX}$ , to avoid overfitting oscillations close to each other as individual subevents. This requirement should not affect the number of subevents because 0.5 s is only about 10% and 1% of the rupture duration of M5.5 and M8 earthquakes. ii) Find the seismic moment  $M_N$  and corner frequency  $f_N$  of subevent  $N$  that minimize the least-squares difference between the STF and  $\Omega_{SUM} = \sum_{k=1}^N \Omega_k(t, t_k, f_k, M_k)$  in the time range  $[0, t_{MIN}]$ . iii) Repeat steps i) and ii) gradually adding subevents to  $\Omega_{SUM}$  until the last subevent  $N_{ev}$ . We normalize the STFs such that the total integrated area is 1.0 and calculated the residual curve between the STF and  $\Omega_{SUM}$ . We then calculated the integrated area of the residual curve to obtain the misfit. We discard STFs if the misfit is larger than 0.5. Analogous to the estimate of  $M_{STF}$  and  $f_{STF}$  we define  $M_{SUM}$  and  $f_{SUM}$  as the seismic moment and corner frequency of a single Brune pulse that best matches  $\Omega_{SUM}$  in a least-squares sense.

144

## 2.2 Source Time Functions as a sum of two Brune pulses

145

146

We derive for the first time the source time functions and source spectra of earthquakes with multiple subevents whose spectra are described by the Brune model. We focus on

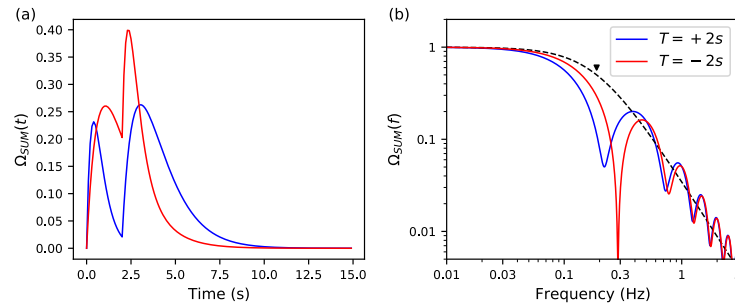
147 earthquakes with two subevents. As shown in section 3.2, two-subevents earthquakes account for  
 148 43% of the SCARDEC dataset. The expression of source time functions can also be extended to  
 149 earthquakes with three or more subevents. We write the source time function of an earthquake  
 150 with two subevents as

$$151 \quad \Omega_{SUM}(t) = \Omega_L(t, t_L, f_L, M_L) + \Omega_S(t, t_S, f_S, M_S) \quad (4)$$

152 where the parameters  $t_L$ ,  $f_L$ , and  $M_L$  and the parameters  $t_S$ ,  $f_S$ , and  $M_S$  are the onset times, corner  
 153 frequencies, and seismic moments of the large and small subevents  $\Omega_L$  and  $\Omega_S$ , respectively. The  
 154 power spectrum of  $\Omega_{SUM}$  for two pulses is

$$155 \quad \Omega_{SUM}^2(f) = \frac{M_L^2}{k_L^2} + \frac{M_S^2}{k_S^2} + \frac{2M_S M_L}{k_S k_L} \cos\{2\pi f(t_L - t_S) + \alpha_L - \alpha_S\} \quad (5)$$

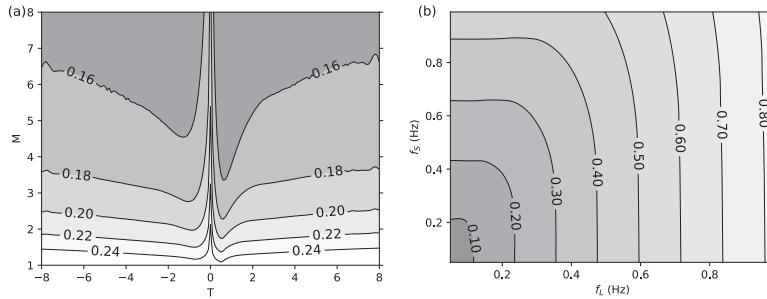
156 where  $k_L = 1 + f^2/f_L^2$ ,  $k_S = 1 + f^2/f_S^2$ ,  $\sin^2 \alpha_L = (k_L - 1)/k_L$ , and  $\sin^2 \alpha_S = (k_S - 1)/k_S$ .  
 157 The first and second terms in (5) are Brune spectra with different low-frequency plateaus and  
 158 corner frequencies that determine the onset of the spectral fall off. The third term represents  
 159 oscillations in the spectrum with periods determined by  $T$  and the phase shifts determined by  $f_L$   
 160 and  $f_S$ . We reduce the number of free parameters to four by considering the moment ratio  $M =$   
 161  $M_L/M_S$  and the onset time difference  $T = t_L - t_S$  of the largest and smallest subevents instead of  
 162  $M_L$ ,  $M_S$ ,  $t_L$ , and  $t_S$  individually.



163  
 164 Figure 2. (a)  $\Omega_{SUM}$  for a sum of two Brune pulses. The large and small subevents have corner frequencies  
 165 of 0.15 Hz and 0.40 Hz, respectively. The moment ratio  $M = M_L/M_S = 3$ . In cases 1 (red) and 2 (blue), the  
 166 largest pulse is the first and second in the sequence so  $T = -2$  s and  $T = +2$  s, respectively. (b) Amplitude  
 167 spectra (solid lines) of the STFs with corresponding colors shown in (a). The dashed line is the spectrum  
 168 of a single-pulse Brune source that best matches  $\Omega_{SUM}$  in a least-squares sense. They are virtually the  
 169 same for  $T = -2$  s and  $T = +2$  s. The corner frequency of this Brune source is  $f_{SUM} = 0.19$  Hz.

170 Figure 2 illustrates the typical form of  $\Omega_{SUM}$  in the time (Figure 2a) and frequency  
 171 (Figure 2b) domains.  $\Omega_{SUM}$  has two subevents with corner frequencies  $f_L = 0.15$  Hz and  $f_S = 0.40$   
 172 Hz and a moment ratio  $M = 3$ . We consider  $T = -2$  s and  $T = +2$  s for which the large subevent  
 173 precedes and succeeds the small subevent by two seconds, respectively (Figure 2a). The order of  
 174 the small and the large subevent can significantly change the shape of the STF and its peak  
 175 values. For example, when  $T = -2$  s, the two maxima in the STF are similar but for  $T = +2$  s, the  
 176 second maximum is 60% higher than the first one. The spectra for  $T = -2$  s and  $T = +2$  s have

177 local minima at different frequencies, and they converge and decay approximately proportional  
 178 to  $f^2$  at frequencies higher than about 0.5 Hz (Figure 2b). The Brune pulse that optimally fits  
 179  $\Omega_{SUM}$  has a corner frequency  $f_{SUM} = 0.19$  Hz for both  $T = -2$  s and  $T = +2$  s, about two times  
 180 lower than  $f_S$ . The location of the first spectral minimum and the spectral decay at high  
 181 frequencies depend on the values of  $f_L$ ,  $f_S$ ,  $M$ , and  $T$ .



182

183 Figure 3. (a) Contour plot of the corner frequency  $f_{SUM}$  as a function of  $T$  and  $M$ . The subevent corner  
 184 frequencies are  $f_L = 0.15$  Hz and  $f_S = 0.40$  Hz. (b) Contour plot of  $f_{SUM}$  as a function of  $f_L$  and  $f_S$ . The  
 185 moment ratio and onset time difference of the two subevents are  $T = 2$  s and  $M = 3$ .

186 Figure 3a shows how  $f_{SUM}$  varies as a function of  $T$  and  $M$  for ranges we resolve for the  
 187 majority of STFs in the SCARDEC catalog with two subevents. As in Figure 2,  $f_L$  is 0.15 Hz and  
 188  $f_S$  is 0.40 Hz. For high values of  $M$ ,  $f_{SUM}$  approaches  $f_L$  because the largest of the two subevents  
 189 dominates  $\Omega_{SUM}$ . For values of  $M$  near 1 and for  $T$  near 0,  $f_{SUM}$  is intermediate between  $f_L$  and  
 190  $f_S$ . The asymmetry of  $f_{SUM}$  about  $T = 0$  indicates that  $f_{SUM}$  depends on the order of the large and  
 191 small subevents in the STF, especially when the onset time difference between the subevents is  
 192 small. The asymmetry originates from a phase shift of  $2(\alpha_L - \alpha_S)$  when the sign of  $T$  changes  
 193 (see (5)), which is the strongest when  $M$  is high. Figure 3b shows how  $f_{SUM}$  varies with subevent  
 194 corner frequencies  $f_L$  and  $f_S$ . We find that  $f_{SUM}$  is more related to  $f_L$  than  $f_S$  when  $M = 3$  and  $T =$   
 195  $2$ .  $f_{SUM}$  is closer to the smaller one of  $f_L$  and  $f_S$  and increases with either of them.

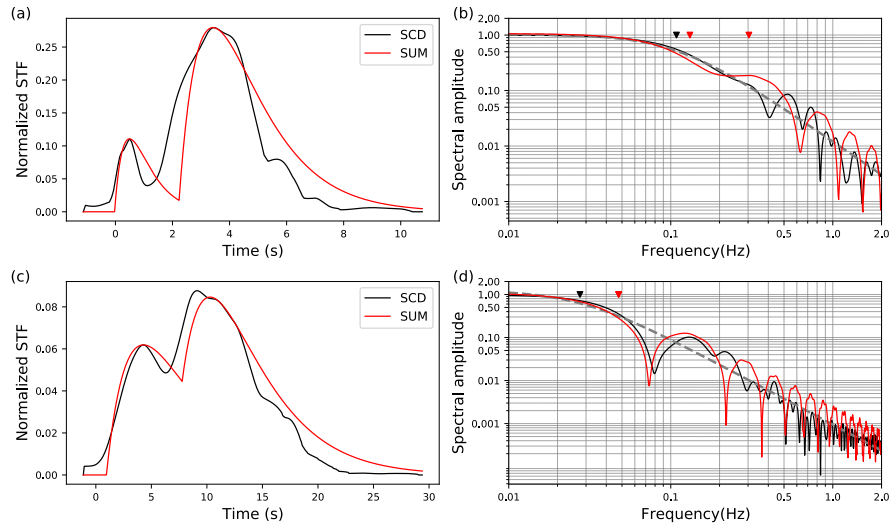
### 196 3 Analysis

#### 197 3.1 The SCARDEC catalog

198 The SCARDEC catalog with source information of hundreds of earthquakes facilitates  
 199 our exploration. Although it does not include constraints on fault slip distribution such as the  
 200 finite-fault modeling databases developed by Ye et al. (2016) and Hayes (2017), it is an order of  
 201 magnitude larger. The SCARDEC analysis is based on the analysis of the waveforms of the  
 202 teleseismic body-wave phases P, PcP, PP, ScS, and SH and their surface reflected phases to  
 203 maximize the range of wave take-off angles in the analysis and thus resolution. There are no  
 204 simplifications regarding the spatial-temporal complexity of the rupture process, so differences  
 205 of the STFs at different stations may capture rupture directivity. However, we use the average of  
 206 the STFs from all stations as an estimate of the overall time dependence of moment rate. The  
 207 SCARDEC catalog has been used in determining the variations of strain drop, stress drop, and

208 radiated energy with depth, magnitude, and tectonic settings (Vallée, 2013; Courboux et al.,  
 209 2016; Chounet & Vallée, 2018; Denolle, 2018; Yin et al., 2021), as well as inversions for rupture  
 210 velocity and rupture direction (Chounet et al., 2018).

211 We decompose STFs of Mw 5.5–8.0 earthquakes between 1992–2017 in the SCARDEC  
 212 catalog. Out of 3,348 earthquakes, 1,640 earthquakes (49%) have two or more subevents. Danré  
 213 et al. (2019) identified a higher percentage of earthquakes with multiple subevents (81%) most  
 214 likely because the Gaussian model describes the source with three free parameters in contrast to  
 215 the two free parameters in the Brune model. Nevertheless, both studies indicate that at least half  
 216 of moderate to large earthquakes are complex.



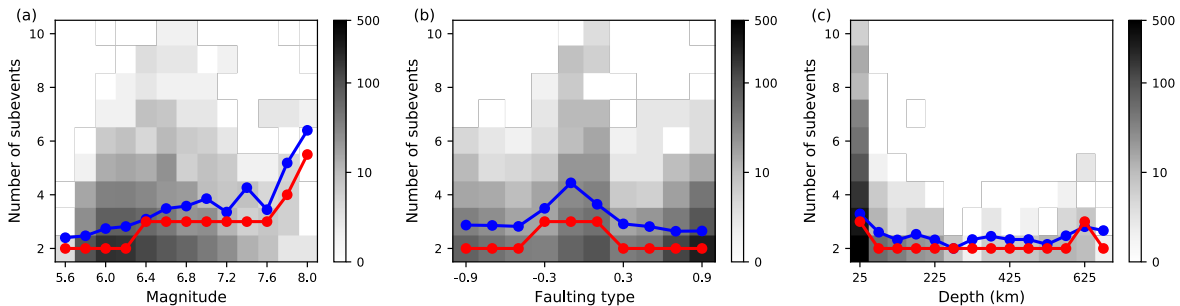
217  
 218 Figure 4. (a) Normalized STFs of the Caroline Islands Mw 6.2 earthquake on December 8, 2017 from the  
 219 SCARDEC dataset (black line) and the best-fitting sum  $\Omega_{SUM}$  of two Brune subevents (red line). (b) The  
 220 spectra of the STF (black line),  $\Omega_{STF}$  (dashed line) and  $\Omega_{SUM}$  (red line). The corner frequency  $f_{STF} = 0.11$   
 221 Hz is marked by a black reversed triangle. The corner frequencies  $f_L = 0.13$  Hz and  $f_S = 0.30$  Hz are  
 222 marked by red reversed triangles. (c) and (d) are the same as (a) and (b) but for the southern Chile Mw 7.6  
 223 earthquake on December 25, 2016, with corner frequencies  $f_{STF} = 0.028$  Hz,  $f_L = 0.048$  Hz, and  $f_S =$   
 224  $0.048$  Hz and  $M = 1.08$ .

225 As an example, Figures 4a and 4c shows the reconstructed STFs (i.e.,  $\Omega_{SUM}$ ) and the  
 226 original STFs of the December 8, 2017 Mw 6.2 earthquake in Caroline Islands and of the  
 227 December 25, 2016 Mw 7.6 earthquake in southern Chile. Figures 4b and 4d show their spectra  
 228  $\Omega_{STF}$  and  $\Omega_{SUM}$ . For the Caroline Islands earthquake, we determine that  $\Omega_{SUM}$  is a sum of two  
 229 Brune sources with a moment ratio of 5.75 and with corner frequencies of 0.13 Hz ( $f_L$ ) and 0.30  
 230 Hz ( $f_S$ ). The large subevent occurred 2.3 seconds after the small subevent. The misfit between  
 231 the normalized STF and  $\Omega_{SUM}$  is 32.8%. The corner frequency is inferred to be 0.11 Hz, slightly  
 232 lower than  $f_L$ , because the largest subevent represents more than 85% of the total moment. The  
 233 observed and synthetic STFs release 90% of the total moment at 6.6 s and 7.8 s. The southern  
 234 Chile earthquake is also decomposed into two Brune sources although it has a longer source

235 duration. For this event, the onset time difference  $T = +6.82$  s, and the moment ratio  $M = 1.08$   
 236 with a misfit of 18.7%. The corner frequencies  $f_L$  and  $f_S$  are both 0.048 Hz and much larger than  
 237 the inferred earthquake corner frequency (0.028 Hz) because the two subevents have similar  
 238 moments. The observed and synthetic STFs release 90% of the total moment at 17.0 s and 19.3 s,  
 239 respectively. We note that the synthetic source duration is larger than the observed source  
 240 duration since the fixed Brune STF decreases slower than the observed STF. Compared to Figure  
 241 4d, spectra in Figure 4b have an extra plateau at 0.2 – 0.3 Hz because of the large difference  
 242 between  $f_L$  and  $f_S$ .

### 243 3.2 Analysis of SCARDEC source time functions

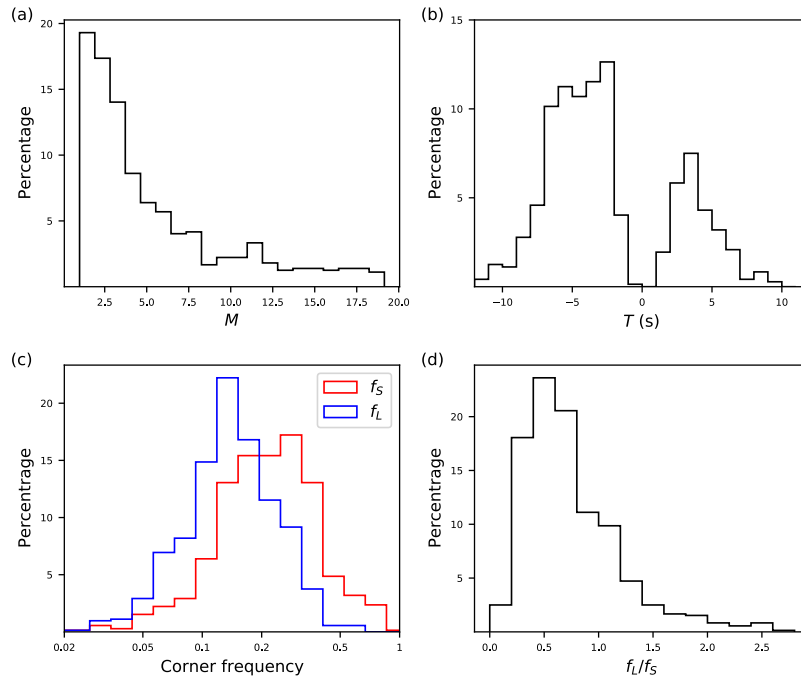
244 Figure 5 summarizes how the number of subevents varies with moment magnitude, focal  
 245 mechanism, and source depth. It suggests that the number of subevents increases with moment  
 246 magnitude in the range of 5.5–8.0 (Figure 5a) and that strike-slip earthquakes are more complex  
 247 than dip-slip earthquakes (Figure 5b). Earthquakes that have 8 or more subevents are all strike-  
 248 slip earthquakes. This is in agreement with the previous study by Danré et al. (2019), indicating  
 249 that the correlation of source complexity with magnitude and faulting type, as quantified by the  
 250 number of subevents, is a robust characteristic of the SCARDEC catalog and weakly influenced  
 251 by the assumed source model for the subevent. We also find that shallow (< 50 km) and very  
 252 deep (> 600 km) earthquakes have more subevents than earthquakes between 50 and 600 km  
 253 depth (Figure 5c). Patterns in Figure 5b and 5c are also observed in Yin et al. (2021).



254  
 255 Figure 5. Contour plot of the number of earthquakes. The y-axis shows the number of subevents in the  
 256 STF up to 10. The x-axis indicates the earthquake’s moment magnitude (a), faulting type (b), and focal  
 257 depth (c). The values of faulting type range from -1 (normal faulting) to 0 (strike-slip faulting) to +1  
 258 (reverse faulting) following the quantification by Shearer et al., (2006). Blue and red circles signify means  
 259 and medians determined for bins of  $\pm 0.1$  (moment magnitude),  $\pm 0.1$  (faulting type), and  $\pm 25$  km (focal  
 260 depth).

### 261 3.3 Analysis of source time functions with two subevents

262

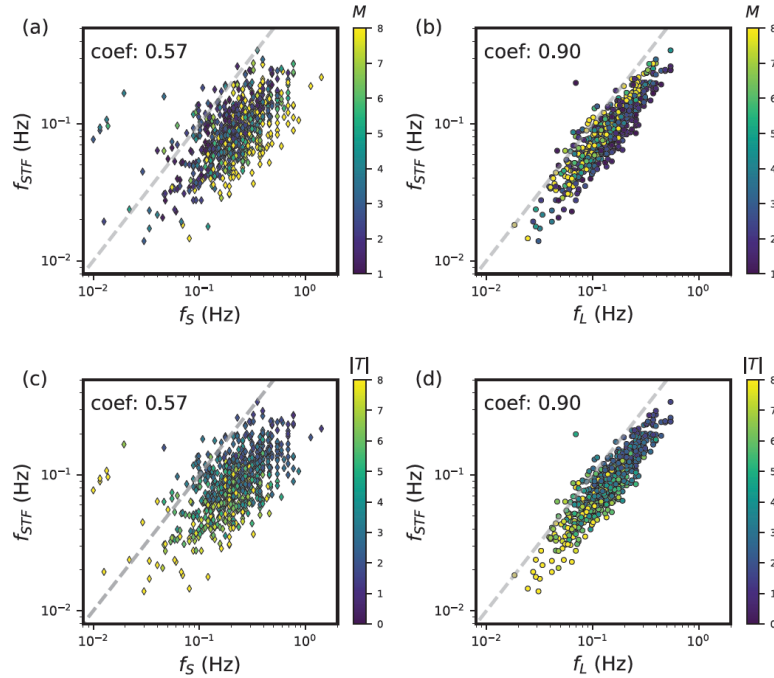


263

264 Figure 6. Histograms of (a) moment ratio  $M = M_L/M_S$ , (b) onset time difference  $T = t_L - t_S$ , (c) corner  
 265 frequency of the largest subevent  $f_L$  and of the smallest subevent  $f_S$  (d) ratio of  $f_L$  to  $f_S$  for 714 STFs with  
 266 two subevents in the SCARDEC catalog.

267 From the 1,640 multi-subevent STFs in the SCARDEC catalog, 714 STFs (43%) have  
 268 two subevents, more than the sum of the number of earthquakes with three (361), four (198), and  
 269 five (104) subevents. Since two-subevents earthquakes are most common and the simplest  
 270 scenario of complex earthquakes, our analysis focuses on earthquakes with two subevents.

271 The magnitude range of two-subevents earthquakes is Mw 5.7-8.0. The ratio  $M$  is lower  
 272 than 8 for about 75% of the STFs (Figure 6a) and the absolute onset time difference  $T$  is between  
 273 2.0 and 8.0 s for about 80% of the STFs (Figure 6b).  $T$  is negative for 521 STFs, suggesting the  
 274 largest subevent precedes the smallest subevent more often. The corner frequency  $f_L$  of the large  
 275 subevent has a median value of 0.14 Hz, higher than the corner frequency  $f_S$  of the small  
 276 subevent that has a median of 0.21 Hz (Figure 6c), consistent with the common observation that  
 277 smaller events have higher corner frequencies.  $f_L/f_S$  has a median of 0.65 (Figure 6d), with 76%  
 278 values smaller than 1.0, which is consistent with the common observation that smaller events  
 279 tend to have higher corner frequencies.



280

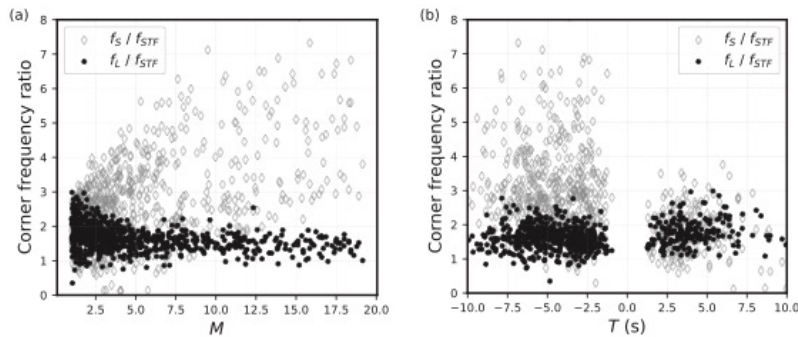
281 Figure 7. (a) and (b) shows the corner frequency  $f_{STF}$  as a function of the corner frequency  $f_S$  and  $f_L$   
 282 color-coded by moment ratio  $M$ . (c) and (d) shows the corner frequency  $f_{STF}$  as a function of the corner  
 283 frequency  $f_S$  and  $f_L$  color-coded by absolute onset time difference  $|T|$ . The dashed lines indicate a 1:1  
 284 correlation.

285 In Figure 7 we evaluate the significance of the corner frequency  $f_{STF}$  of the 714  
 286 SCARDEC STFs that are decomposed to have two subevents. The correlation between  $f_{STF}$  and  
 287  $f_L$  (Figures 7b and 7d) is higher than the correlation between  $f_{STF}$  and  $f_S$  (Figure 7a and 7c) with  
 288 cross-correlation coefficients of about 0.90 and 0.57, respectively. This indicates that the large  
 289 subevent determines  $f_{STF}$  the most, which agrees with the theoretical results shown in Figure 2b.  
 290 We find that the corner frequencies of subevents  $f_S$  and  $f_L$  are overall higher than the earthquake  
 291 corner frequency  $f_{STF}$ . The correlations between  $f_{STF}$  and subevent corner frequencies further  
 292 support the finding of Danré et al. (2019) that the moment of subevents is correlated to the  
 293 moment of the main event for self-similar earthquakes.

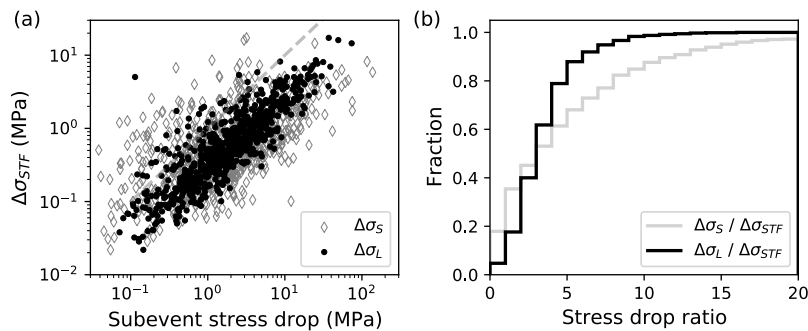
294 The color-coding in Figures 7a and 7b indicates that with increasing moment ratio  $M$ , the  
 295 difference between  $f_{STF}$  and  $f_S$  tends to increase while the difference between  $f_{STF}$  and  $f_L$  tends  
 296 to decrease, which is also observed in Figure 2a. The plot of the  $f_S/f_{STF}$  and  $f_L/f_{STF}$  ratios in  
 297 Figure 8a further illustrate this. The limitation in frequency bandwidth could result in increasing  
 298  $f_S/f_{STF}$  with  $M$  if  $f_S$  is high enough, but here most corner frequency estimates are within 0.7 Hz  
 299 which should be resolvable given a time step of 0.005s. Beginning with a similar spread at  $M =$   
 300 1, the scatter in  $f_S/f_{STF}$  increases with increasing  $M$ , while  $f_L/f_{STF}$  tends to cluster to a value of  
 301 about 1.2. Although  $f_L/f_{STF}$  is expected to approach 1 theoretically for the highest values of  $M$ ,  
 302 we suspect that the misfit of the decomposition of STF renders  $\Omega_{SUM}$  to have a slightly different  
 303 frequency content than  $\Omega_{STF}$ . Figures 7c and 7d show that for an increasing absolute onset time

304 difference  $|T|$  between subevents,  $f_{STF}$  and  $f_L$  decreases. This is consistent with the fact that  $|T|$   
 305 controls the total source duration, which is inversely proportional to the corner frequency of the  
 306 Brune pulse. Therefore,  $f_{STF}$  and the closely correlated  $f_L$ , are inversely proportional to  $|T|$ ,  
 307 whereas the change of  $f_S$  with  $|T|$  is less obvious due to high scatter.

308 Figure 8b shows an asymmetry in the ratios  $f_S/f_{STF}$  and  $f_L/f_{STF}$  with reference to  $T = 0$ ,  
 309 implying that the order of the large and small subevents of subevent (i.e.,  $T > 0$  and  $T < 0$ ) has an  
 310 influence on the corner frequency estimates. The variation in  $f_S/f_{STF}$  for  $T < 0$  is two times  
 311 higher than for  $T > 0$ , suggesting that  $f_S$  is similar to  $f_{STF}$  and better constrained if the small  
 312 subevent precedes that large subevent. The variation in ratio  $f_L/f_{STF}$  does not change with  $T$ , but  
 313 the mean value of  $f_L/f_{STF}$  for  $T < 0$  is slightly smaller than  $f_L/f_{STF}$  for  $T > 0$  (1.60 versus 1.79).  
 314 Since the absolute value of  $T$  is higher than 1 for most STF in the SCARDEC catalog (see  
 315 Figure 6b), the relatively small influence of  $T$  on  $f_L/f_{STF}$  is consistent with Figure 2a, where we  
 316 found that  $f_{STF}$  depends strongly on  $T$  only when  $|T| < 1$ .  
 317



318  
 319 Figure 8. The ratio between corner frequencies  $f_L$  (solid black circles) and  $f_S$  (gray open diamonds) to  
 320  $f_{STF}$  as a function of moment ratio  $M$  (a) and onset time difference  $T$  (b).  
 321



322  
 323 Figure 9. (a) Average stress drop  $\Delta\sigma_{STF}$  as a function of the stress drop  $\Delta\sigma_L$  (circles) and  $\Delta\sigma_S$  (diamonds)  
 324 of the large and small subevents, respectively. (b) Cumulative fraction of the ratios  $\Delta\sigma_L/\Delta\sigma_{STF}$  (black  
 325 line) and  $\Delta\sigma_S/\Delta\sigma_{STF}$  (grey line).

326 The Brune model relates the corner frequency  $f_c$  to stress drop  $\Delta\sigma$  assuming a circular  
 327 crack model:

$$\Delta\sigma = \frac{7M_0f_c^3}{16\beta^3k^3} \quad (6)$$

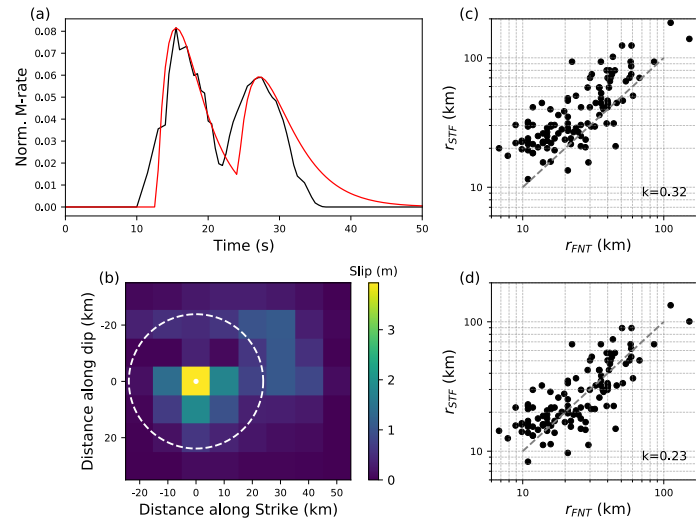
328 Here  $k$  is a constant and  $\beta$  is the shear wave velocity (Madariaga, 1976). In (6),  $\Delta\sigma$  represents  
 329 the average stress change on the fault plane. Analogous to our definitions for  $f_{STF}$ , we define  
 330  $\Delta\sigma_{STF}$  as the average stress drop determined for the SCARDEC STF. Further, we define  $\Delta\sigma_L$  and  
 331  $\Delta\sigma_S$  and  $M_L$  and  $M_S$  as the stress drops and seismic moments of the large and small subevents,  
 332 respectively. The shear wave velocity is referred from PREM (Dziewonski & Anderson, 1981)  
 333 model. We assume the rupture velocity is about  $0.7\beta$  (Ye et al., 2016; Hayes, 2017; Chounet et  
 334 al., 2017). Note that the value of  $k$  is related to the spherical average of the corner frequency, and  
 335 is different for P- and S-waves (Sato & Hirasawa, 1973; Madariaga, 1976; Kaneko & Shearer,  
 336 2014, 2015; Wang & Day, 2017). Since SCARDEC STFs are obtained by averaging P and S  
 337 waves after removal of Green's functions, we set  $k$  as 0.32 according to Sato & Hirasawa (2017)  
 338 and Kaneko & Shearer (2015).  $\Delta\sigma_{STF}$ ,  $\Delta\sigma_L$ , and  $\Delta\sigma_S$  are proportional to the cube of  $f_{STF}$ ,  $f_L$ , and  
 339  $f_S$ . Therefore, as for  $f_L$ ,  $f_S$ , and  $f_{STF}$ , the correlation between  $\Delta\sigma_{STF}$  and  $\Delta\sigma_L$  is higher than the  
 340 correlation between  $\Delta\sigma_{STF}$  and  $\Delta\sigma_S$  (Figure 9a). The correlation of Brune stress drop estimates  
 341 with the largest asperity supports the usage of the moment-weighted stress drop and the energy-  
 342 based stress drop (Noda et al., 2013).  $\Delta\sigma_L$  and  $\Delta\sigma_S$  are also larger than  $\Delta\sigma_{STF}$  (Figure 9b). For  
 343 50% of the STFs  $\Delta\sigma_L$  and  $\Delta\sigma_S$  are larger than  $\Delta\sigma_{STF}$  by a factor of 4, and stress drops of the small  
 344 subevents is an order of magnitude higher than the overall stress drop for 20% of the earthquakes  
 345 in the SCARDEC catalog (see also Figure 6c).

## 347 4 Discussion

### 348 4.1 Comparison with finite-fault inversion results

349 Through the STFs decomposition, we find that the corner frequency of the master event  
 350 is more related to the largest subevent. STFs show temporal behavior of the rupture moment  
 351 release, however, provide no spatial information of the rupture process. Thus, we compare  
 352 subevent corner frequencies measured from STFs with rupture dimensions of subevents  
 353 estimated from finite-fault inversion datasets. Ye et al. (2016) applied finite-fault inversion to  
 354 teleseismic P waveforms of 114 earthquakes larger than Mw7.0. We fit the source spectra of  
 355 STFs from finite-fault inversion to the Brune source model to estimate the corner frequency of  
 356 the earthquake  $f_{STF}$  and convert it to rupture radius following  $r_{STF} = k\beta/f_{STF}$ , where  $k$  is a  
 357 constant and  $\beta$  the shear wave velocity. Assuming an average crustal shear-wave velocity ( $\beta =$   
 358 3.5 km/s), the rupture velocity used by Ye et al. (2016) (2.5 km/s) is 70% of the shear wave  
 359 velocity. We use corresponding  $k$  values of P waves from Sato & Hirasawa (1973) and Kaneko  
 360 & Shearer (2015). We then decompose STFs to estimate the moment of the largest subevent.  
 361 Assuming that the largest subevent with the highest slip can be approximated by a circle, we use  
 362 the moment release distribution to find the radius  $r_{FNT}$  when the total moment release within the  
 363 circle is equal to the largest subevent. As an example, Figures 10a and 10b display the STF for

364 the 2014 April 18, Guerrero earthquake and its slip map where the circle with a radius of  $r_{FNT} =$   
 365 24 km outlines the region of slip of the largest subevent.



366  
 367 Figure 10. (a) The normalized source time function and (b) slip distribution in Ye et al. (2016) for the  
 368 April, 18, 2014 Mw7.3 Guerrero earthquake. The black curve in (a) is the STF from finite-fault inversion  
 369 and the red curve is its decomposition into two Brune sources. The white dashed circle in (b) with a radius  
 370  $r_{FNT} = 24$  km signifies the rupture area of the largest subevent. The best-fit Brune corner frequency is  
 371  $f_{STF} = 0.04$  Hz. (c) Radius  $r_{STF}$  converting from  $f_{STF}$  using  $k = 0.32$  as a function of the largest subevent  
 372 radius  $r_{FNT}$  measured from finite-fault inversion. The grey dashed line signifies a 1:1 relation. (d) Same  
 373 as (c) but with  $k = 0.23$ .

374 Figures 10c and 10d show that  $r_{STF}$  are positively correlated with  $r_{FNT}$ . The radius  $r_{STF}$   
 375 depends linearly on  $k$ . For  $k = 0.23$  (Sato & Hirasawa, 1973)  $r_{STF}$  is about 30% higher than for  $k$   
 376  $= 0.32$  (Kaneko & Shearer, 2015), but  $k$  has no influence on the correlation between  $r_{STF}$  and  
 377  $r_{FNT}$ . A change of 10% moment would result in approximate 10% change of the radius. We note  
 378 that the estimation of  $r_{FNT}$  is rough because the rupture areas of subevents may not be circles.  
 379 Nevertheless, the proportionality of  $r_{STF}$  and  $r_{FNT}$  supports our conclusion that the largest  
 380 subevent strongly influences estimates of the earthquake corner frequency and rupture  
 381 dimension, and estimates of earthquake corner frequency represent rupture dimensions of the  
 382 largest subevent.

#### 383 4.2 Observed stress drop variability

384 The stress drops estimated from the SCARDEC STFs dataset have a standard deviation  
 385 of about a factor of 3.5. This standard deviation is close to the factor-of-three variability of stress  
 386 drop estimated from the SCARDEC STFs by Courboux et al. (2016), and is similar to the  
 387 variability of stress drop estimated from the moment rate functions of earthquakes in dynamic  
 388 rupture simulations (Galovic and Valentova, 2020). Allmann and Shearer (2009) obtained a  
 389 stress drop variability of about a factor of 4.5 using a spectral fitting method based on global  
 390 eGfs. Our results show that the stress drop variability may be a consequence of earthquake

391 complexity. Whereas for a simple source, the stress drop inferred from the Brune source corner  
 392 frequency represents the average stress drop on the fault plane, the stress drop of a complex  
 393 rupture with multiple subevents is influenced strongly by the largest subevent. Therefore,  
 394 earthquakes with the same magnitudes can have varying stress drops depending on the source  
 395 complexity and the largest subevent dimension. This could explain the significant higher  
 396 variability of stress drop estimated from source time functions of simulated ruptures than the  
 397 variability of stress drop prescribed in dynamic rupture models (Cotton et al., 2003; Lin and  
 398 Lapusta, 2018; Gallovic and Valentova, 2020). A better understanding of the source of stress  
 399 drop variability helps to predict ground velocity and acceleration after major earthquakes, which  
 400 are essential for the seismic hazard assessment.

401 We note that, in addition to the source complexity, the simplicity of the Brune source  
 402 model itself can also lead to a systematic deviation of the stress drop estimation. The Brune  
 403 source model is widely applied due to its simplicity, but also suffers from inaccurate  
 404 representation for complex earthquake sources. Although we obtain similar distributions of  
 405 subevent numbers using the Brune source model as Danré et al. (2019) who used the Gaussian  
 406 source model, the variation of stress drop estimates is cubed when stress drop is converted from  
 407 corner frequency estimates. Apart from the model choice, the quality of dataset (Green's  
 408 function removal in SCARDEC STFs), the frequency bandwidth, and the spectral fit method all  
 409 contribute to the corner frequency and stress drop variation.

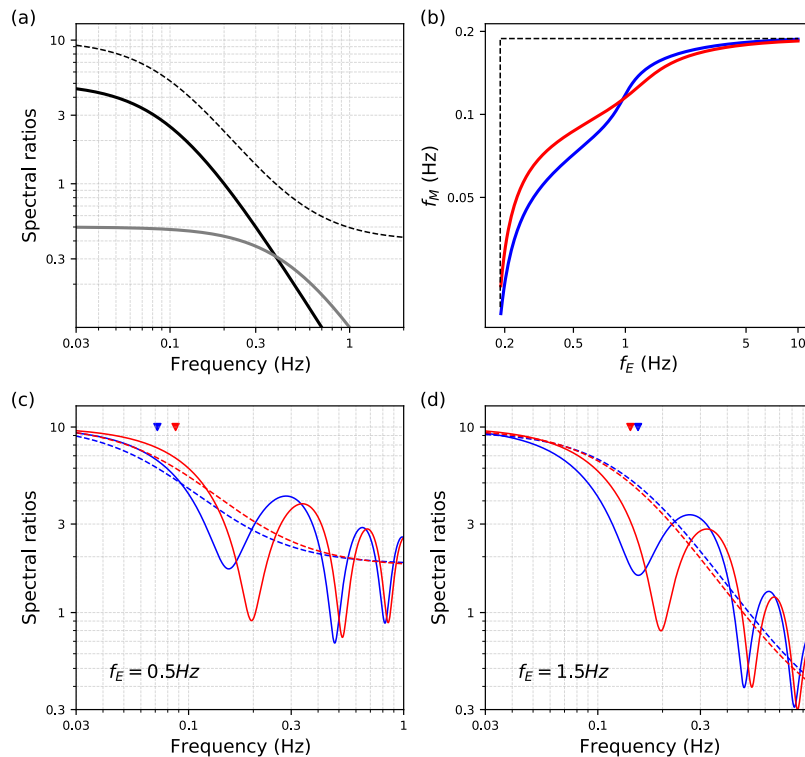
#### 410 4.3 Application to spectral ratios

411 Since the spectral ratio method is frequently used to estimate corner frequencies (e.g.,  
 412 Abercrombie, 2015; Huang et al, 2016; Uchide and Imanishi, 2016; Liu et al, 2020) we explore  
 413 the resolution of the corner frequencies of a large earthquake (referred to as the master event  
 414 hereafter) after dividing its spectrum  $\Omega_M$  by the spectrum  $\Omega_E$  of a co-located but smaller  
 415 earthquake. The spectral ratio method isolates the source term of the master event, because for  
 416 the same station the propagation and receiver effects are the same in  $\Omega_M$  and  $\Omega_E$ . Therefore, the  
 417 smaller earthquake can be regarded as the empirical Green's function (referred to as eGf  
 418 hereafter).

419 Assuming Brune sources as in eq. (1), the spectral ratio is  $\Omega_{RATIO}(f, f_{RATIO}, M_{RATIO}) =$   
 420  $\Omega_M(f, f_M, M_M)/\Omega_E(f, f_E, M_E)$ , where,  $M_M, M_E, f_M, f_E$  are seismic moments and corner  
 421 frequencies of the master event and the eGf. The spectral ratio  $\Omega_{RATIO}$  has a seismic moment  
 422 ratio  $M_{RATIO}$  and a first corner frequency  $f_{RATIO}$  (i.e., master event corner frequency inferred  
 423 from the spectral ratio method). Note that the spectral ratio also has a second corner frequency  
 424 that corresponds to the eGf corner frequency. If  $f_E$  is much higher than  $f_M$ ,  $\Omega_{RATIO}$  is equivalent  
 425 to  $\Omega_M$  and  $f_M$  is equivalent to  $f_{RATIO}$ . If  $f_E$  is similar to  $f_M$ ,  $\Omega_{RATIO}$  decays more slowly at high  
 426 frequencies than  $\Omega_M$ . There are two approaches to get the source spectral information  $M_M$  and  
 427  $f_M$ : 1) removing the Green's function and performing spectral fitting (e.g., Shearer et al., 2007,  
 428 2009), and 2) fitting the spectral ratio of two Brune models based on empirical Green's function

429 (e.g. Abercrombie, 1995; Abercrombie, 2014, 2015), with two approaches benchmarked in  
 430 Shearer et al. (2019).

431 We show the spectra and the spectral ratio of the second spectral ratio approach in Figure  
 432 11a. Figures 11c and 11d demonstrate this for the master events used in Figure 2 (i.e., events  
 433 composed of two subevents with onset time difference of  $T = -2$  s and  $T = +2$  s) that have a  
 434 corner frequency  $f_M = 0.19$  Hz for both cases of  $T$ . The eGfs used to compute  $\Omega_{RATIO}$  are single-  
 435 pulse Brune sources with corner frequencies of 0.5 Hz (Figure 11c) and 1.5 Hz (Figure 11d). In  
 436 both cases,  $f_{RATIO}$  is inferred to be lower than  $f_M$  because the first oscillation in the spectral  
 437 ratios causes an earlier and faster decay near  $f_M$  (Figure 2b). This decreasing effect on  $f_{RATIO}$  is  
 438 stronger when the eGf has a corner frequency closer to  $f_M$ . For  $f_E$  higher than 1 Hz,  $f_{RATIO}$   
 439 approaches  $f_M$  asymptotically (Figure 11b). In addition, the sequence of the large and small  
 440 subevents affects  $f_{RATIO}$ . The master event corner frequency is inferred to be larger when large  
 441 subevent precedes small subevent ( $T = -2$  s).



442

443 Figure 11. (a) Spectra of the master event (black solid) with  $f_M = 0.1$  Hz,  $M_M = 5$  and the eGf (grey solid)  
 444 with  $f_E = 0.5$  Hz,  $M_E = 0.5$  Hz as well as their spectral ratio (dashed line). (c) Spectral ratios for  $T = +2$  s  
 445 (blue) and  $T = -2$  s (red) when  $f_E = 0.5$  Hz. The master event has the same spectra as the spectra shown in  
 446 Figure 2. The corners  $f_M$  of the spectral ratio  $\Omega_M$  are indicated by reversed triangles for the cases where  
 447 the large subevent precedes (in red) or succeeds (in blue) the small subevent by 2 s. (d) Same as (a) for  $f_E$   
 448 = 1.5 Hz. (b)  $f_M$  as a function of  $f_E$  for  $T = +2$  s (blue) and  $T = -2$  s (red). The horizontal and vertical  
 449 black dashed lines indicate the corner frequency  $f_M = 0.19$  Hz of the master event.

450 There is an upper bound of the frequencies (2 Hz in our case) in the source spectrum used  
451 for the fitting of the Brune source spectrum. Because  $\Omega_M$  and  $\Omega_E$  decay identically above  $f_E$ , the  
452 first corner of a spectral ratio is primarily determined by signals at frequencies lower than  $f_E$  that  
453 is usually smaller than the upper frequency range. For multi-subevent earthquakes, oscillations at  
454 frequencies smaller than  $f_E$  dominate the modeling of spectral ratios. Theoretically, if the eGf  
455 has the form of a single-pulse Brune spectrum, its corner frequency does not strongly influence  
456 the estimate of the corner frequency of the master event. For complex master events, however,  
457 oscillations at frequencies smaller than  $f_E$ , rather than the overall fall-off control the fitting. As  
458  $f_E$  decreases, we are more likely to fit the first oscillation which has a corner frequency smaller  
459 than the master event. Therefore, the spectral ratio method yields a larger variance in the  
460 estimated corner frequency than the direct fitting of earthquake source spectra when the master  
461 event consists of multiple subevents.

#### 462 4.4 More complex spectral models

463 It is necessary to differentiate two subevent corner frequencies in our analysis from the  
464 double-corner frequency model (Archuleta and Ji, 2016; Denolle and Shearer, 2016; Uchide and  
465 Imanishi, 2016; Wang & Day, 2017; Ji & Archuleta, 2021). The double-corner frequency has an  
466 additional corner compared to the Brune source model and variable fall-off rates, so it can better  
467 model complex source spectra at high frequency. The underlying physics of an additional corner  
468 is an extra time scale relating to one of the following source properties: the slip rise time (Brune,  
469 1970), the time between the starting and stopping phases (Luco, 1985), the spacing of barriers  
470 and asperities (Denolle and Shearer, 2016), and the superposition of two subevents (Atkinson,  
471 1993). Our analysis is based on the Brune source model, so we only estimate a single corner  
472 frequency of the master event, which characterizes the whole earthquake. Similarly, subevent  
473 corner frequencies only characterize the source properties of subevents separately.

#### 474 4.5 Comparison with previous SCARDEC decomposition results

475 Our decomposition approach is the same as Danré et al. (2019), but we assume the Brune  
476 source instead of the Gaussian source used in their analysis. The Gaussian source model is  
477 described by three source parameters and thus more adaptable than the Brune source model with  
478 two parameters. Though Danré et al. (2019) resolved more subevents than found in this study,  
479 the relative number of subevents per faulting type are consistent in two studies, indicating that  
480 source models have no effect on the analysis. Both Danré et al. (2019) and our study showed that  
481 the smallest earthquakes have the fewest subevents, but both studies are limited by the  
482 decomposition method and the resolvable frequency bandwidth of SCARDEC STFs which are  
483 obtained from teleseismic body-wave phases. Because teleseismic waveforms above 0.5 Hz have  
484 relatively low signal-to-noise ratios and STFs are averaged over stations, high-frequency  
485 contents are deficient in SCARDEC STFs. Additionally, the decomposition method requires  
486 subevents to have moments that are at least 10% of the total moment. Therefore, it is likely that  
487 smaller subevents were missed by our analysis. The spectral analysis of regional and local  
488 seismograms would enable a study of the relationships of corner frequencies and rupture

489 dimensions of subevents of Mw 3–4 earthquakes to test whether small earthquakes are as  
490 complex as large earthquakes (e.g., Fischer, 2005; Abercrombie, 2014, Ruhl et al., 2017).

#### 491 4.6 Limited frequency range of the SCARDEC STFs

492 SCARDEC STFs above 0.5 Hz is inaccurate due to the wave attenuation and wave  
493 propagation complexities as well as averaging of spectra from global stations. This inherent lack  
494 of high frequency of SCARDEC STFs reduces our resolution of subevents for smaller  
495 earthquakes, and would lead to a constant resolvable subevent magnitude for different  
496 earthquake magnitudes. However, our decomposition results show that the magnitudes of  
497 smallest resolvable subevents increase with earthquake magnitude, and the resolvable magnitude  
498 range of subevents is almost the same ( $\sim 1.3$ ) for various earthquake magnitudes (Figure S1),  
499 consistent with Danré et al. (2019). It suggests that our decomposition method, which requires a  
500 minimum moment rate of subevents according to the STF, controls the resolution of subevents.  
501 Therefore, the observed increasing number of subevents with earthquake magnitude is not an  
502 artifact.

### 503 5 Conclusions

504 We use SCARDEC source time functions to investigate how estimates of the corner  
505 frequency of earthquakes with multiple subevents are biased by assuming a simple Brune source.  
506 By decomposing SCARDEC STFs, we find more than half of Mw 5.5–8.0 earthquakes have  
507 multiple subevents. We derive theoretical solutions of the source spectrum for an earthquake  
508 with two Brune-type subevents. The theoretical derivation demonstrates that the earthquake  
509 corner frequency correlates better with the corner frequency of the large subevent than the small  
510 subevent. In both synthetic tests and the analysis of the SCARDEC catalog, earthquake corner  
511 frequency approaches the largest subevent corner frequency as the moment ratio between  
512 subevents increases, whereas the onset time difference between subevents has a minor effect  
513 with slight asymmetry. The positive correlation is also observed for earthquake rupture  
514 dimension estimated from its corner frequency and rupture dimension of the largest subevent  
515 estimated from finite-fault inversion. Our findings suggest that the corner frequency estimates  
516 may reflect the stress change of the largest asperity instead of the average stress drop on the  
517 whole rupture area, which helps to explain the commonly observed large variance of stress drop  
518 estimates.

### 519 Acknowledgments, Samples, and Data

520 This study is sponsored by the National Science Foundation award EAR–2019379. We thank  
521 Martin Vallée for advice on the SCARDEC catalog of source time functions. The SCARDEC  
522 catalog is available at: <http://scardec.projects.sismo.ipgp.fr/>. All data and codes used in this paper  
523 will be available through Deep Blue Data repository (<https://doi.org/10.7302/4ga6-8574>).

524

525 **References**

- 526 Abercrombie, R. E. (1995). Earthquake source scaling relationships from – 1 to 5 ML using  
527 seismograms recorded at 2.5-km depth. *Journal of Geophysical Research: Solid Earth*,  
528 *100*(B12), 24015-24036.
- 529 Abercrombie, R. E. (2014). Stress drops of repeating earthquakes on the San Andreas fault at  
530 Parkfield. *Geophysical Research Letters*, *41*(24), 8784-8791.
- 531 Abercrombie, R. E. (2015). Investigating uncertainties in empirical Green's function analysis of  
532 earthquake source parameters. *Journal of Geophysical Research: Solid Earth*, *120*(6), 4263-  
533 4277.
- 534 Abercrombie, R. E., Chen, X., & Zhang, J. (2020). Repeating Earthquakes with Remarkably  
535 Repeatable Ruptures on the San Andreas Fault at Parkfield. *Geophysical Research Letters*,  
536 *47*(23), e2020GL089820.
- 537 Allmann, B. P., & Shearer, P. M. (2009). Global variations of stress drop for moderate to large  
538 earthquakes. *Journal of Geophysical Research: Solid Earth*, *114*(B1).
- 539 Ando, R., & Kaneko, Y. (2018). Dynamic rupture simulation reproduces spontaneous multifault  
540 rupture and arrest during the 2016 Mw 7.9 Kaikoura earthquake. *Geophysical Research Letters*,  
541 *45*(23), 12-875.
- 542 Archuleta, R. J., & Ji, C. (2016). Moment rate scaling for earthquakes  $3.3 \leq M \leq 5.3$  with  
543 implications for stress drop. *Geophysical Research Letters*, *43*(23), 12-004.
- 544 Atkinson, G. M. (1993). Earthquake source spectra in eastern North America. *Bulletin of the*  
545 *Seismological Society of America*, *83*(6), 1778-1798.
- 546 Baltay, A., Ide, S., Prieto, G., & Beroza, G. (2011). Variability in earthquake stress drop and  
547 apparent stress. *Geophysical Research Letters*, *38*(6).
- 548 Beresnev, I., & Atkinson, G. (2001). Subevent structure of large earthquakes—A ground-motion  
549 perspective. *Geophysical Research Letters*, *28*(1), 53-56.
- 550 Boatwright, J. (1984). The effect of rupture complexity on estimates of source size. *Journal of*  
551 *Geophysical Research: Solid Earth*, *89*(B2), 1132-1146.
- 552 Branch, M. A., Coleman, T. F., & Li, Y. (1999). A subspace, interior, and conjugate gradient  
553 method for large-scale bound-constrained minimization problems. *SIAM Journal on Scientific*  
554 *Computing*, *21*(1), 1-23.
- 555 Chen, X., & Shearer, P. M. (2011). Comprehensive analysis of earthquake source spectra and  
556 swarms in the Salton Trough, California. *Journal of Geophysical Research: Solid Earth*,  
557 *116*(B9).

- 558 Chounet, A., & Vallée, M. (2018). Global and interregion characterization of subduction  
559 interface earthquakes derived from source time functions properties. *Journal of Geophysical*  
560 *Research: Solid Earth*, 123(7), 5831-5852.
- 561 Chounet, A., Vallée, M., Causse, M., & Courboux, F. (2018). Global catalog of earthquake  
562 rupture velocities shows anticorrelation between stress drop and rupture velocity.  
563 *Tectonophysics*, 733, 148-158.
- 564 Cooley, J. W., & Tukey, J. W. (1965). An algorithm for the machine calculation of complex  
565 Fourier series. *Mathematics of computation*, 19(90), 297-301.
- 566 Cotton, F., Archuleta, R., & Causse, M. (2013). What is sigma of the stress drop?. *Seismological*  
567 *Research Letters*, 84(1), 42-48.
- 568 Courboux, F., Vallée, M., Causse, M., & Chounet, A. (2016). Stress-drop variability of shallow  
569 earthquakes extracted from a global database of source time functions. *Seismological Research*  
570 *Letters*, 87(4), 912-918.
- 571 Danré, P., Yin, J., Lipovsky, B. P., & Denolle, M. A. (2019). Earthquakes within earthquakes:  
572 Patterns in rupture complexity. *Geophysical Research Letters*, 46(13), 7352-7360.
- 573 Das, S., & Aki, K. (1977). Fault plane with barriers: a versatile earthquake model. *Journal of*  
574 *geophysical research*, 82(36), 5658-5670.
- 575 Denolle, M. A., & Shearer, P. M. (2016). New perspectives on self-similarity for shallow thrust  
576 earthquakes. *Journal of Geophysical Research: Solid Earth*, 121(9), 6533-6565.
- 577 Dziewonski, A. M., & Anderson, D. L. (1981). Preliminary reference Earth model. *Physics of the*  
578 *earth and planetary interiors*, 25(4), 297-356.
- 579 Fischer, T. (2005). Modelling of multiple events using empirical Green's functions: method,  
580 application to swarm earthquakes and implications for their rupture propagation. *Geophysical*  
581 *Journal International*, 163(3), 991-1005.
- 582 Gallovič, F., & Valentová, L. (2020). Earthquake stress drops from dynamic rupture simulations  
583 constrained by observed ground motions. *Geophysical Research Letters*, 47(4), e2019GL085880.
- 584 García, D., Singh, S. K., Herráiz, M., Pacheco, J. F., & Ordaz, M. (2004). Inslab earthquakes of  
585 central Mexico: Q, source spectra, and stress drop. *Bulletin of the Seismological Society of*  
586 *America*, 94(3), 789-802.
- 587 Hayes, G. P. (2017). The finite, kinematic rupture properties of great-sized earthquakes since  
588 1990. *Earth and Planetary Science Letters*, 468, 94-100.
- 589 Huang, Y., & Ampuero, J. P. (2011). Pulse-like ruptures induced by low-velocity fault zones.  
590 *Journal of Geophysical Research: Solid Earth*, 116(B12).

- 591 Huang, Y., Beroza, G. C., & Ellsworth, W. L. (2016). Stress drop estimates of potentially  
592 induced earthquakes in the Guy-Greenbrier sequence. *Journal of Geophysical Research: Solid*  
593 *Earth*, 121(9), 6597-6607.
- 594 Ji, C., & Archuleta, R. J. (2021). Two Empirical Double-Corner-Frequency Source Spectra and  
595 Their Physical Implications. *Bulletin of the Seismological Society of America*, 111(2), 737-761.
- 596 Kaneko, Y., & Shearer, P. M. (2015). Variability of seismic source spectra, estimated stress  
597 drop, and radiated energy, derived from cohesive-zone models of symmetrical and asymmetrical  
598 circular and elliptical ruptures. *Journal of Geophysical Research: Solid Earth*, 120(2), 1053-  
599 1079.
- 600 Lay, T., Kanamori, H., & Ruff, L. (1982). The asperity model and the nature of large subduction  
601 zone earthquakes.
- 602 Lay, T., & Kanamori, H. (1981). An asperity model of large earthquake sequences.
- 603 Li, Y., Doll Jr, C., & Toksöz, M. N. (1995). Source characterization and fault plane  
604 determination for  $M_b L_g = 1.2$  to 4.4 earthquakes in the Charlevoix Seismic Zone, Quebec,  
605 Canada. *Bulletin of the Seismological Society of America*, 85(6), 1604-1621.
- 606 Lin, Y. Y., & Lapusta, N. (2018). Microseismicity simulated on asperity-like fault patches: On  
607 scaling of seismic moment with duration and seismological estimates of stress drops.  
608 *Geophysical Research Letters*, 45(16), 8145-8155.
- 609 Liu, M., Huang, Y., & Ritsema, J. (2020). Stress Drop Variation of Deep-Focus Earthquakes  
610 Based on Empirical Green's Functions. *Geophysical Research Letters*, 47(9), e2019GL086055.
- 611 Luco, J. E. (1985). On strong ground motion estimates based on models of the radiated spectrum.  
612 *Bulletin of the Seismological Society of America*, 75(3), 641-649.
- 613 Madariaga, R. (1976). Dynamics of an expanding circular fault. *Bulletin of the Seismological*  
614 *Society of America*, 66(3), 639-666.
- 615 Noda, H., Lapusta, N., & Kanamori, H. (2013). Comparison of average stress drop measures for  
616 ruptures with heterogeneous stress change and implications for earthquake physics. *Geophysical*  
617 *Journal International*, 193(3), 1691-1712.
- 618 Oth, A. (2013). On the characteristics of earthquake stress release variations in Japan. *Earth and*  
619 *Planetary Science Letters*, 377, 132-141.
- 620 Papageorgiou, A. S., & Aki, K. (1983). A specific barrier model for the quantitative description  
621 of inhomogeneous faulting and the prediction of strong ground motion. I. Description of the  
622 model. *Bulletin of the Seismological Society of America*, 73(3), 693-722.
- 623 Prieto, G. A., Froment, B., Yu, C., Poli, P., & Abercrombie, R. (2017). Earthquake rupture below  
624 the brittle-ductile transition in continental lithospheric mantle. *Science Advances*, 3(3),  
625 e1602642.

- 626 Purvance, M. D., & Anderson, J. G. (2003). A comprehensive study of the observed spectral  
627 decay in strong-motion accelerations recorded in Guerrero, Mexico. *Bulletin of the Seismological*  
628 *Society of America*, 93(2), 600-611.
- 629 Ruhl, C. J., Abercrombie, R. E., & Smith, K. D. (2017). Spatiotemporal variation of stress drop  
630 during the 2008 Mogul, Nevada, earthquake swarm. *Journal of Geophysical Research: Solid*  
631 *Earth*, 122(10), 8163-8180.
- 632 Sato, T., & Hirasawa, T. (1973). Body wave spectra from propagating shear cracks. *Journal of*  
633 *Physics of the Earth*, 21(4), 415-431.
- 634 Shearer, P. M., Prieto, G. A., & Hauksson, E. (2006). Comprehensive analysis of earthquake  
635 source spectra in southern California. *Journal of Geophysical Research: Solid Earth*, 111(B6).
- 636 Shearer, P. M., Abercrombie, R. E., Trugman, D. T., & Wang, W. (2019). Comparing EGF  
637 methods for estimating corner frequency and stress drop from P wave spectra. *Journal of*  
638 *Geophysical Research: Solid Earth*, 124(4), 3966-3986.
- 639 Sotiriadis, D., Margaris, B., Klimis, N., & Sextos, A. (2021). Implications of high-frequency  
640 decay parameter, “ $\kappa$ -kappa”, in the estimation of kinematic soil-structure interaction effects. *Soil*  
641 *Dynamics and Earthquake Engineering*, 144, 106665.
- 642 Trugman, D. T., Dougherty, S. L., Cochran, E. S., & Shearer, P. M. (2017). Source spectral  
643 properties of small to moderate earthquakes in southern Kansas. *Journal of Geophysical*  
644 *Research: Solid Earth*, 122(10), 8021-8034.
- 645 Uchide, T., & Imanishi, K. (2016). Small earthquakes deviate from the omega-square model as  
646 revealed by multiple spectral ratio analysis. *Bulletin of the Seismological Society of America*,  
647 106(3), 1357-1363.
- 648 Ulrich, T., Gabriel, A. A., Ampuero, J. P., & Xu, W. (2019). Dynamic viability of the 2016 Mw  
649 7.8 Kaikōura earthquake cascade on weak crustal faults. *Nature communications*, 10(1), 1-16.
- 650 Vallée, M. (2013). Source time function properties indicate a strain drop independent of  
651 earthquake depth and magnitude. *Nature communications*, 4(1), 1-6.
- 652 Vallée, M., & Douet, V. (2016). A new database of source time functions (STFs) extracted from  
653 the SCARDEC method. *Physics of the Earth and Planetary Interiors*, 257, 149-157.
- 654 Wang, E., Rubin, A. M., & Ampuero, J. P. (2014). Compound earthquakes on a bimaterial  
655 interface and implications for rupture mechanics. *Geophysical Journal International*, 197(2),  
656 1138-1153.
- 657 Wang, Y., & Day, S. M. (2017). Seismic source spectral properties of crack-like and pulse-like  
658 modes of dynamic rupture. *Journal of Geophysical Research: Solid Earth*, 122(8), 6657-6684.
- 659 Wu, Q., Chapman, M., & Chen, X. (2018). Stress-drop variations of induced earthquakes in  
660 Oklahoma. *Bulletin of the Seismological Society of America*, 108(3A), 1107-1123.

661 Ye, L., Lay, T., Kanamori, H., & Rivera, L. (2016). Rupture characteristics of major and great  
662 ( $M_w \geq 7.0$ ) megathrust earthquakes from 1990 to 2015: 1. Source parameter scaling  
663 relationships. *Journal of Geophysical Research: Solid Earth*, *121*(2), 826-844.

664 Yin, J., Li, Z., & Denolle, M. A. (2021). Source time function clustering reveals patterns in  
665 earthquake dynamics. *Seismological Society of America*, *92*(4), 2343-2353.

666 Yu, H., Harrington, R. M., Kao, H., Liu, Y., Abercrombie, R. E., & Wang, B. (2020). Well  
667 proximity governing stress drop variation and seismic attenuation associated with hydraulic  
668 fracturing induced earthquakes. *Journal of Geophysical Research: Solid Earth*, *125*(9),  
669 e2020JB020103.

670